IOPscience iopscience.iop.org

Home Search Collections Journals About Contact us My IOPscience

Microstructure dependence of leakage and resistive switching behaviours in Ce-doped $BiFeO_3$ thin films

This content has been downloaded from IOPscience. Please scroll down to see the full text.

2011 J. Phys. D: Appl. Phys. 44 415104

(http://iopscience.iop.org/0022-3727/44/41/415104)

View the table of contents for this issue, or go to the journal homepage for more

Download details:

IP Address: 210.72.19.250
This content was downloaded on 01/11/2015 at 06:42

Please note that terms and conditions apply.

J. Phys. D: Appl. Phys. **44** (2011) 415104 (7pp) doi:10.1088/0022-3727/44/41/415104

Microstructure dependence of leakage and resistive switching behaviours in Ce-doped $BiFeO_3$ thin films

Xiaojian Zhu[1,2], Fei Zhuge[1,2], Mi Li[1,2], Kuibo Yin[1,2], Yiwei Liu[1,2], Zhenghu Zuo[1,2], Bin Chen[1,2] and Run-Wei Li[1,2]

[1] Key Laboratory of Magnetic Materials and Devices, Ningbo Institute of Material Technology and Engineering, Chinese Academy of Sciences, Ningbo 315201, People's Republic of China
[2] Zhejiang Province Key Laboratory of Magnetic Materials and Application Technology, Ningbo Institute of Material Technology and Engineering, Chinese Academy of Sciences, Ningbo 315201, People's Republic of China

E-mail: zhugefei@nimte.ac.cn and runweili@nimte.ac.cn

Received 13 March 2011, in final form 27 August 2011
Published 26 September 2011
Online at stacks.iop.org/JPhysD/44/415104

Abstract
The leakage current and resistive switching (RS) of Ce-doped $BiFeO_3$ (BCFO) films prepared by the sol–gel method at various annealing temperatures are investigated. With increasing annealing temperature, BCFO changes from an amorphous structure to a crystalline structure, while the leakage current increases due to an increase in the carrier mobility as well as an increase in the oxygen vacancy concentration. Bipolar RS behaviours are observed in BCFO films, which can be attributed to the formation/rupture of metal filaments due to the diffusion of the top electrodes under a bias voltage. With increasing annealing temperature, the forming voltage decreases, while no obvious changes are observed in resistances in both ON and OFF states and programming voltages, demonstrating that the RS occurs in a confined region. The pristine BCFO shows Schottky emission conduction behaviour, while Ohmic conduction and space charge limited conduction dominate in ON and OFF states, respectively.

(Some figures in this article are in colour only in the electronic version)

1. Introduction

Resistive random access memory (RRAM), which is based on resistive switching (RS) induced by external electrical stimulations, has attracted considerable attention due to its potential applications in next generation nonvolatile memory. RS phenomena have been reported in a wide variety of materials including organic materials [1, 2], amorphous Si [3], carbon-based materials [4–6], binary oxides such as NiO [7], Cu_xO [8], ZrO_2 [9], WO_3 [10], and HfO_2 [11] as well as complex oxides such as $Pr_{1-x}Ca_xMnO_3$ [12], $La_{0.7}Ca_{0.3}MnO_3$ [13] and $SrTiO_3$ [14]. Recently, RS effect has been found in $BiFeO_3$ (BFO) films [15, 16]. Multiferroic material BFO is considered as a promising candidate for memory and sensor materials due to its distinctive properties such as large spontaneous polarization, high Curie temperature ($T_C \sim 1103$ K), and high Neel temperature ($T_N \sim 643$ K) [17, 18]. However, one of the main drawbacks that could limit the applications of this material is the high leakage current density which could be attributed to the presence of Fe^{3+} cations with a non-d^0 electronic configuration [19]. It has been found that the appropriate replacement of Bi^{3+} at the *A* site with aliovalent atoms such as Ce [20], La [21] and Nb [22], or Fe^{3+} at the *B* site with aliovalent atoms such as Sc [23], Ti [24], Cr [25] and Mn [26], or doping aliovalent impurities on both *A* and *B* sites of BFO [27–29] could effectively reduce the leakage current of BFO films by suppressing the formation of oxygen vacancies and valence fluctuation of Fe ions. Among these dopants, Ce should be a promising one since the ionic radii of Ce^{3+} (1.18 Å) and Ce^{4+} (1.02 Å) are closer to that of Bi^{3+} (1.20 Å). Appropriate Ce cations might be used to substitute for *A* site Bi^{3+} in the BFO matrix and Ce cations could stabilize oxygen octahedron that helps decrease Bi volatilization [30]. Wang *et al* have reported that 5 mol% Ce doping can reduce

 © 2011 IOP Publishing Ltd Printed in the UK & the USA

the leakage current density of BFO films by two orders of magnitude [20].

Yin *et al* reported that the RS phenomenon can only be observed in BFO films prepared by the sol–gel method and annealed at and above 650 °C, while BFO films annealed below 650 °C do not show RS behaviour [15]. However, Chen *et al* observed RS in BFO films annealed at 500 °C and 550 °C while no RS behaviour can be found in BFO annealed at 450 °C [16]. The RS behaviour is attributed to the diffusion of oxygen vacancies in BFO. Therefore, the microstructure should play an important role in the RS behaviour of BFO. However, the effect of microstructure on the RS of BFO is still not clear. In this paper, the leakage current and RS behaviour in Cu/Ce-doped BFO (BCFO)/Pt sandwiched structures are investigated with BCFO films annealed at temperatures in the range 450–650 °C. It is found that the leakage current increases with annealing temperature due to an increase in the carrier mobility as well as an increase in the oxygen vacancy concentration. All the BCFO films can show RS behaviour. The forming voltage decreases with annealing temperature while the programming voltages and resistances in both ON and OFF states do not change obviously. The RS can be attributed to the formation and rupture of metal filaments with a diameter of about 11 nm due to the diffusion of the top electrodes.

2. Experimental

The $Bi_{0.95}Ce_{0.05}FeO_3$ films were fabricated on commercially available $Pt/Ti/SiO_2/Si$ substrates by the sol–gel process. Bismuth nitrate $[Bi(NO_3)_3 \cdot 5H_2O]$, cerium nitrate $[Ce(NO_3)_3 \cdot 6H_2O]$ and ferric nitrate $[Fe(NO_3)_3 \cdot 9H_2O]$ were used as the starting materials to prepare the BCFO precursor solution. Excess 2 mol% $Bi(NO_3)_3 5H_2O$ was used to attempt to compensate for the expected loss of volatile Bi during the following heat treatment. The BCFO thin films were deposited by spin-coating at 1000 rpm for 10 s followed by spin-coating at 5000 rpm for 30 s. Thermal baking was performed at 300 °C for 10 min on a hotplate in air. This process was repeated six times to obtain the desired thickness of the films, and the typical thickness was about 275 nm. These films were then annealed for 10 min at temperatures in the range 450–650 °C. For electrical measurements, Cu top electrodes with a diameter of 200 μm and thickness of 125 nm were deposited at room temperature (RT) by electron beam evaporation with an *in situ* shadow mask.

The crystal structure and microstructure were examined by x-ray diffraction (XRD, Huber six-circle diffractometer) and high-resolution transmission electron microscopy (HRTEM, Tecnai F20, FEI). Atomic force microscopy (AFM, Dimension V, Veeco) was used to detect the surface morphology. The chemical composition and bonding states were measured by x-ray photoelectron spectroscopy (XPS) using a Kratos AXIS ULTRADLD instrument with a monochromic Al K_α x-ray source. The electrical properties of the Cu/BCFO/Pt structures were measured at RT by a Keithley 4200 semiconductor characterization system with voltage sweeping mode. During the measurement, a bias voltage was applied between the top (Cu) and bottom (Pt) electrodes with the latter being grounded. The resistance in the low resistance state of the Cu/BCFO/Pt structures as a function of temperature was studied by a physical property measurement system (PPMS, Quantum Design).

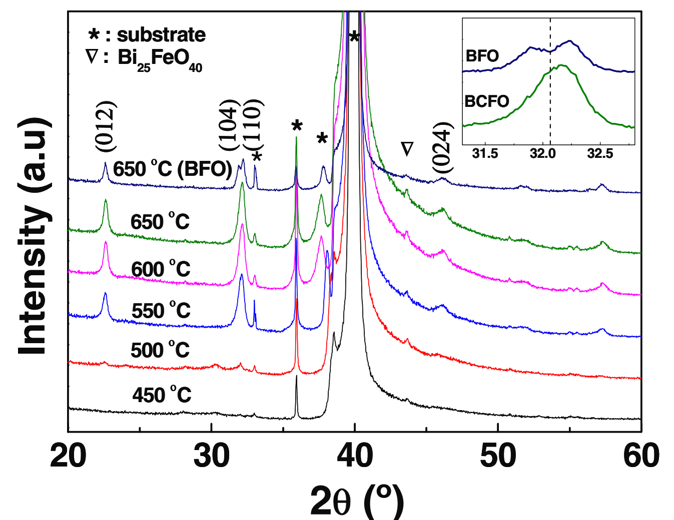

Figure 1. XRD patterns of BCFO films annealed at various temperatures and BFO films annealed at 650 °C. The inset shows the enlarged XRD patterns of BFO and BCFO films annealed at 650 °C.

3. Results and discussion

Figure 1 shows the typical XRD patterns of the BCFO films annealed at various temperatures and pure BFO films annealed at 650 °C. The inset shows the enlarged XRD patterns of the BCFO and BFO films annealed at 650 °C. The BCFO films annealed at 450 °C are amorphous and no XRD peaks of BCFO can be observed. As the annealing temperature increases to 500 °C, the diffraction peaks of BCFO perovskite phase appear indicating that the BCFO films begin to crystallize. The intensity of the BCFO XRD peaks increases with annealing temperature illustrating an improvement in crystallinity. As can be seen from the inset of figure 1, the XRD pattern of BFO around $2\theta = 32°$ shows two diffraction peaks of (1 0 4) and (1 1 0), while these two characteristic peaks merge to a single peak for the BCFO films. This demonstrates that the structure of BFO is changed from rhombohedral to tetragonal due to Ce substitution. The grain size of the BCFO films annealed at temperatures from 500 to 650 °C is estimated by the Scherrer equation, i.e. $D = 0.89\lambda/(\beta \cos\theta)$, where D is the average grain size, λ is the x-ray wavelength, β is the width of the diffraction peak at half of the maximum height and θ is the diffraction angle. The grain size of the BCFO films is found to increase with annealing temperature, i.e. 15.4 nm at 500 °C, 18.5 nm at 550 °C, 18.9 nm at 600 °C and 19.1 nm at 650 °C. The grain size of pure BFO films annealed at 650 °C is calculated to be 34.4 nm, much larger than that of the BCFO films. This indicates that Ce doping can suppress the grain growth of BFO. Figures 2(*a*), (*b*) and (*c*) show the AFM images of the films annealed at 450 °C, 550 °C and 650 °C, respectively. As can be seen, the film surface becomes rough as the temperature increases. The

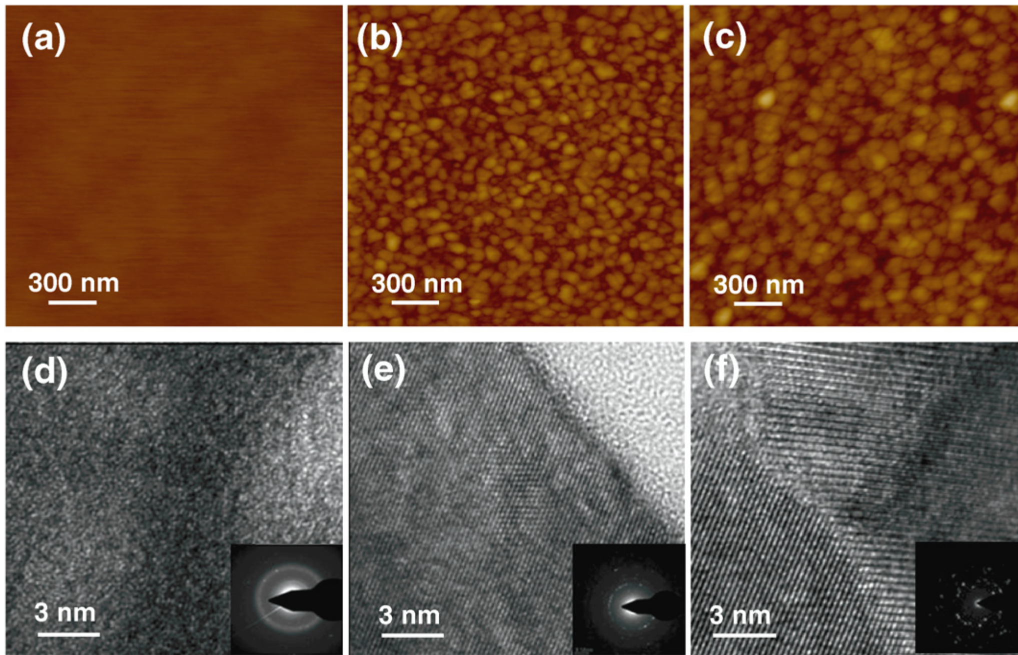

Figure 2. AFM images of BCFO films annealed at (*a*) 450 °C, (*b*) 550 °C and (*c*) 650 °C. HRTEM images of BCFO films annealed at (*d*) 450 °C, (*e*) 550 °C and (*f*) 650 °C. The insets show the corresponding ED images.

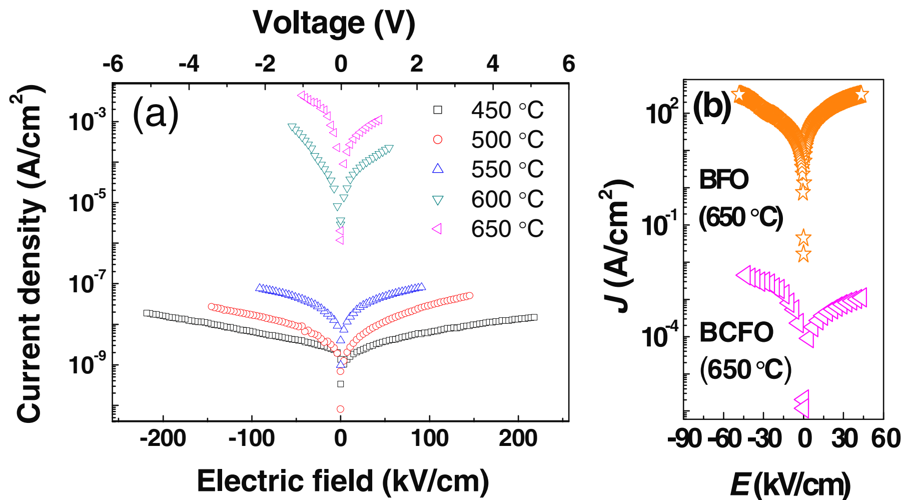

Figure 3. (*a*) Leakage current density–electric field and leakage current density–voltage characteristics of BCFO films prepared at various annealing temperatures. (*b*) J–E curves of BFO and BCFO films annealed at 650 °C.

mean roughness changes from 0.2 nm at 450 °C to 6.9 nm at 650 °C. At the same time, the crystal grain size increases with annealing temperature. Figures 2(*d*), (*e*) and (*f*) show the HRTEM images of the films annealed at 450 °C, 550 °C and 650 °C, respectively. The insets are the corresponding electron diffraction (ED) patterns. As seen from both HRTEM images and ED patterns, the BCFO annealed at 450 °C shows an amorphous structure, while the film annealed at 550 °C shows a mixture of amorphous and crystalline phases and the sample annealed at 650 °C is completely crystallized. Therefore, from the XRD and HRTEM results, we can conclude that the BCFO films vary from an amorphous structure to a mixture of amorphous and crystalline phases and eventually to a fully crystallized phase as annealed at temperatures ranging from 450 to 650 °C.

Figure 3(*a*) displays the typical leakage current density (J) as a function of applied electric field (E) and voltage as well for BCFO annealed at various temperatures. The leakage current is very sensitive to the annealing temperature, i.e. the higher the annealing temperature, the higher is the leakage current. A similar dependence of leakage current on annealing temperature has been reported in BFO and La-doped BFO thin films [15, 31]. It has been ascribed to higher oxygen vacancy concentrations due to more Fe^{2+} ions in the films at higher temperatures [31, 32]. Figure 3(*b*) shows the J–E curves of pure BFO and BCFO films annealed at 650 °C. The leakage current density is reduced by more than four orders of magnitude via Ce doping. To confirm the existence of oxygen vacancies in the BCFO films, XPS measurements were performed. The inset of figure 4 presents the O 1s XPS

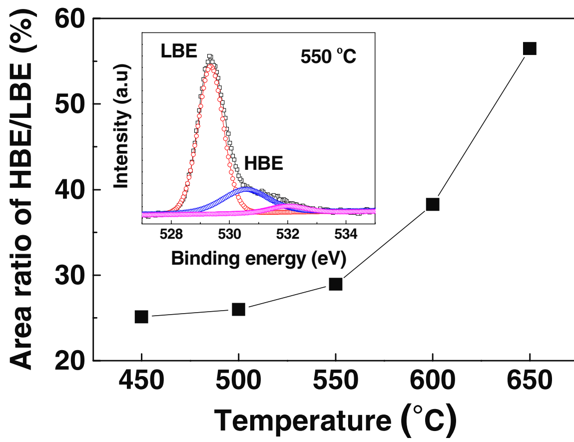

Figure 4. Plot of the area ratio of HBE XPS peak to LBE XPS peak of BCFO versus annealing temperature. The inset shows the XPS spectra of BCFO annealed at 550 °C and the corresponding Gaussian fitting.

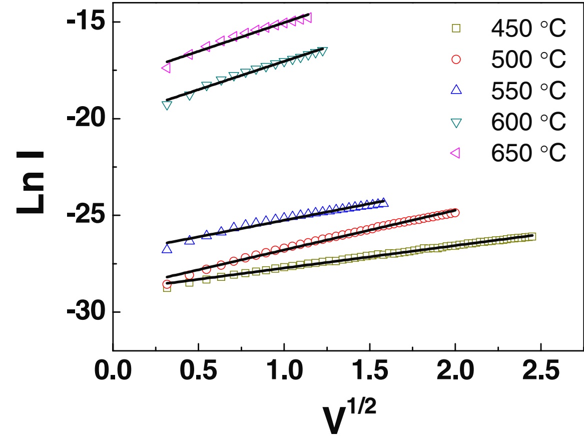

Figure 5. Plot of Ln(I) versus $V^{1/2}$ and linear fittings for BCFO films annealed at various temperatures.

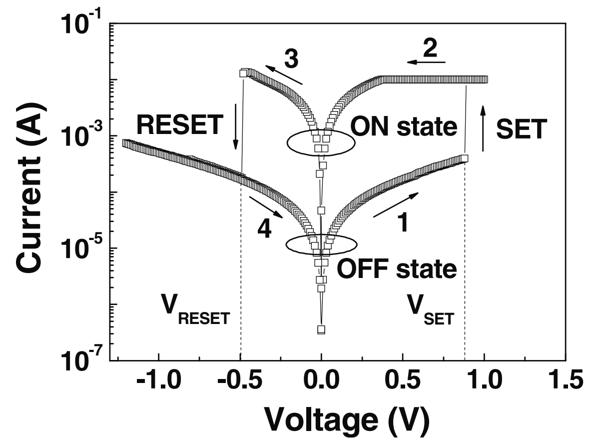

Figure 6. Typical I–V characteristics of BCFO annealed at 500 °C.

spectra of the BCFO films annealed at 550 °C, which show a slightly asymmetric peak close to 530 eV. It can be Gaussian fitted by three symmetrical peaks at 529.4 eV, 530.6 eV and 532.0 eV, which are related to the lattice oxygen, the loss of oxygen and the absorbed oxygen on the surface, respectively. The peaks at 529.4 eV and 530.6 eV are normally assigned as the low binding energy (LBE) peak and high binding energy (HBE) peak, respectively. Figure 4 shows a plot of the area ratio of the HBE peak to the LBE peak versus annealing temperature, indicating that the oxygen vacancy concentration increases with annealing temperature [33]. Therefore, it may be inferred that the larger leakage current density of the BCFO films annealed at a higher temperature originates from a higher oxygen vacancy concentration. However, in our opinion, another important factor contributing to the leakage current variations, i.e. changes in the carrier mobility at different annealing temperatures, should not be neglected. Amorphous phases always have low carrier mobility due to disordered structures which scatter the carriers efficiently. For crystalline phases, the carrier scattering may arise from three parts: grain boundaries, lattice vibrations and ionized impurities. Herein, all BCFO samples have the same Ce doping level. Thus, the mobility variations of crystalline BCFO films should be due to the difference in the carrier scattering by grain boundaries. Based on the analysis above, it can be inferred that the carrier mobility increases with decreasing amorphous phase content, and for completely crystallized samples, the mobility increases with an increase in the grain size (i.e. a decrease in the number of grain boundaries) [34, 35]. In other words, the mobility increases with annealing temperature, in accordance with the leakage current variation. Therefore, it is suggested that the change in the carrier mobility plays an important role in the leakage current variations for the BCFO thin films annealed at different temperatures. In order to study the conduction mechanism in BCFO films, several carrier transport models are used to fit the measured current–voltage (I–V) data, i.e. Schottky emission, space charge limited conduction, Poole–Frenkel emission and Fowler–Nordheim tunnelling. It is found that the I–V characteristics of all the BCFO samples obey the Schottky emission model, i.e. Ln(I) $\propto$ $V^{1/2}$, as shown in figure 5. Similar results were observed in Co-doped and La–Co codoped BFO thin films [36].

Bipolar RS behaviours are observed in BCFO thin films annealed at temperatures in the range 450–650 °C. Figure 6 shows the typical I–V characteristics of the BCFO annealed at 500 °C. Before RS, a forming process is needed to achieve reversible switching loops by applying a certain voltage on the fresh samples. During the forming process, a compliance current of 0.01 A is necessary to prevent the sample from a permanent breakdown. As seen from figure 6, the BCFO switches from the high resistance state (HRS or OFF state) to a low resistance state (LRS or ON state) at about 0.8 V (V_{SET}), and switches from the ON state to the OFF state at about −0.5 V (V_{RESET}).

To understand the conduction and switching mechanisms of BCFO thin films, the I–V curves are plotted in a log–log scale. Figure 7 shows the logarithmic plot and linear fitting of the I–V curves of the samples annealed at different temperatures for the positive voltage sweep regions, while they are similar for the negative branches. As shown in figure 7, the I–V curves of the LRS exhibit a linear Ohmic behaviour with a slope of about 1. This is thought to correspond to the formation of conducting filaments during the SET process.

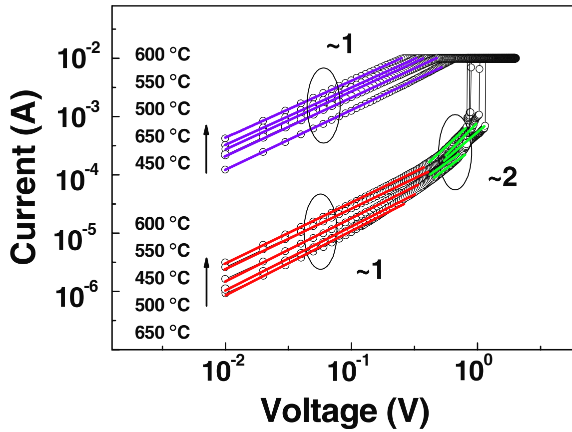

Figure 7. I–V curves of BCFO films annealed at various temperatures plotted in the log–log scale and the linear fitting results in both HRS and LRS.

However, the conduction mechanisms of the HRS are much more complicated. Fitting the results for the HRS suggest that the charge transport behaviour is in good agreement with a trap-controlled space charge limited conduction, which mainly consists of two portions: the Ohmic region ($I \propto V$) and the Child's law region ($I \propto V^2$) [37]. Figure 8(a) shows the top electrode size dependence of the resistances in the HRS (R_{HRS}) and LRS (R_{LRS}) of the BCFO annealed at 600 °C. R_{HRS} clearly increases with a decrease in the electrode area; however, R_{LRS} shows weak dependence on the electrode area. The area-insensitive property of R_{LRS} demonstrates that the RS of the BCFO films is dominated by the conducting-filament mechanism [38]. To confirm the RS mechanism of the BCFO films, R_{LRS} of the Cu/BCFO/Pt device was measured as a function of temperature. Figure 8(b) shows the typical metallic behaviour of R_{LRS}. The metallic conducting behaviour in the LRS confirms the formation of metal filaments in the BCFO films. The temperature dependence of metallic resistance can be written as $R(T) = R_0[1 + \alpha(T - T_0)]$, where R_0 is the resistance at temperature T_0, and α is the temperature coefficient of resistance. By choosing T_0 as 300 K, the α of the filaments is calculated to be about $1.3 \times 10^{-3}\,K^{-1}$, which is close to the value $2.5 \times 10^{-3}\,K^{-1}$ for high-purity Cu nanowires of diameter $\geqslant$15 nm, indicating that the filaments are composed of Cu in metallic states due to the diffusion of the top electrode under a bias voltage [39, 40]. The discrepancy of α is attributed to inevitable defects in the Cu filaments, since the presence of defects can reduce α by shortening the mean free path of electrons [41].

Figure 9(a) shows the relationship between the initial resistance of BCFO and annealing temperature. The initial resistance decreases with annealing temperature. The forming voltage for BCFO is found to have the same tendency, i.e. decreasing with annealing temperature, as shown in figure 9(b). The samples annealed at 550, 600 and 650 °C have mean forming voltages of 2.70, 1.75 and 1.32 V, which are much lower than those (20.8 and 11.6 V) for the samples annealed at 450 and 500 °C. From the XRD patterns (figure 1) and HRTEM images (figures 2(d), (e) and (f)), we can see that the samples annealed at 550, 600 and 650 °C are mainly composed of crystalline phases, while the samples annealed at 450 and 500 °C are mainly composed of the amorphous phase. It is known that extended defects, such as grain boundaries and dislocations, provide easy diffusion paths for oxygen vacancies or metal ions in metallic oxides [42]. Point defects such as oxygen vacancies or metal ions prefer to form and gather around the grain boundaries. Therefore, conducting filaments are apt to form at grain boundaries [43]. The samples annealed at 550, 600 and 650 °C have a large number of grain boundaries, which provide natural channels for filament generation. It results in low forming voltages. Moreover, the forming voltages of the samples annealed at 550, 600 and 650 °C exhibit small fluctuations, while larger fluctuations are observed for the samples annealed at 450 and 500 °C, as shown in figure 9(b). It can also be explained by the existence of grain boundaries for the samples annealed at higher temperatures. Compared with the amorphous phase, the formation of conducting filaments at grain boundaries is less random in the crystalline phases. Figures 9(c) and (d) illustrate the annealing temperature dependence of resistances in the HRS and LRS (R_{HRS} and R_{LRS}) and the programming voltages (V_{SET} and V_{RESET}), respectively. Both resistances and programming voltages show weak dependence on annealing temperature, much different from the variation of the forming voltage. Note that, from figure 9, the resistances in the HRS and LRS are much lower than the initial resistances and the SET voltages are lower than the forming voltages. Therefore, we infer that once the forming process is completed, it is most likely that the local conducting filaments, rather than the bulk region of BCFO, contribute to the RS effectively. During the RESET process, the filaments are broken in the weakest parts while the rest of the filaments remain resulting in much lower R_{HRS} compared with the initial resistances. The following SET process only needs to connect the broken filaments resulting in lower SET voltages compared with the forming voltages. In order to estimate the diameter of the copper filaments, it is assumed that only one complete filament forms in the LRS. The LRS resistance can be written as $R_{LRS} = \rho_{Cu}L/S$, where ρ_{Cu} is the resistivity of copper, L is the filament length and S is the filament cross-sectional area. By choosing $\rho_{Cu} = 1.75 \times 10^{-6}\,\Omega\,cm$, $L = 275$ nm and $R_{LRS} = 50\,\Omega$, S is calculated to be about $9.63 \times 10^{-17}\,m^2$. Thus, the corresponding diameter of the metal filament is estimated to be about 11 nm.

4. Conclusion

For sol–gel prepared BCFO films, as the annealing temperature increases, the crystallinity improves; the leakage current increases due to an increase in both the carrier mobility and oxygen vacancy concentration. The bipolar RS originating from the formation/rupture of metal filaments due to the diffusion of the top electrodes is observed in BCFO annealed at various temperatures. As the annealing temperature increases, the forming voltage reduces, while the programming voltages and resistances in both ON and OFF states do not show any obvious change, demonstrating that the RS occurs in a confined region. It is found that the BCFO before forming shows Schottky emission conduction behaviour while space charge limited conduction dominates in the OFF state.

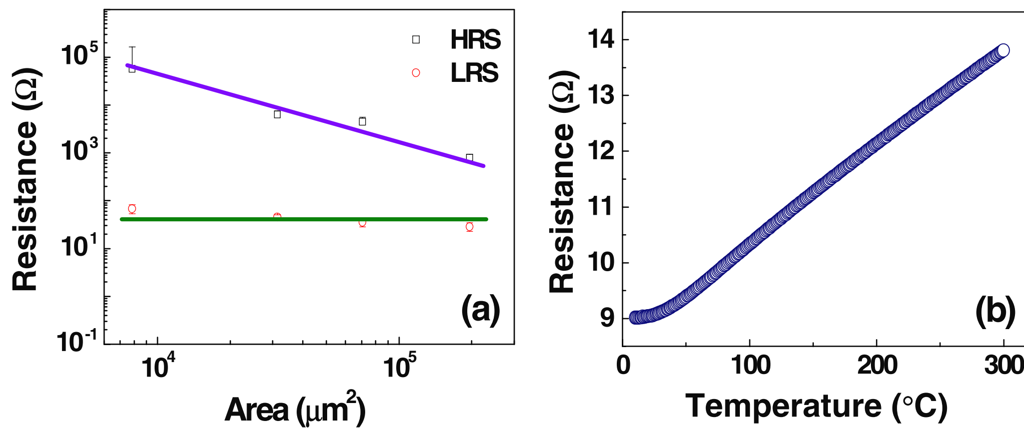

Figure 8. (*a*) Top electrode area dependence of the resistances in HRS and LRS for BCFO annealed at 600 °C. (*b*) Temperature dependence of the resistance in LRS for Cu/BCFO/Pt devices with BCFO annealed at 600 °C.

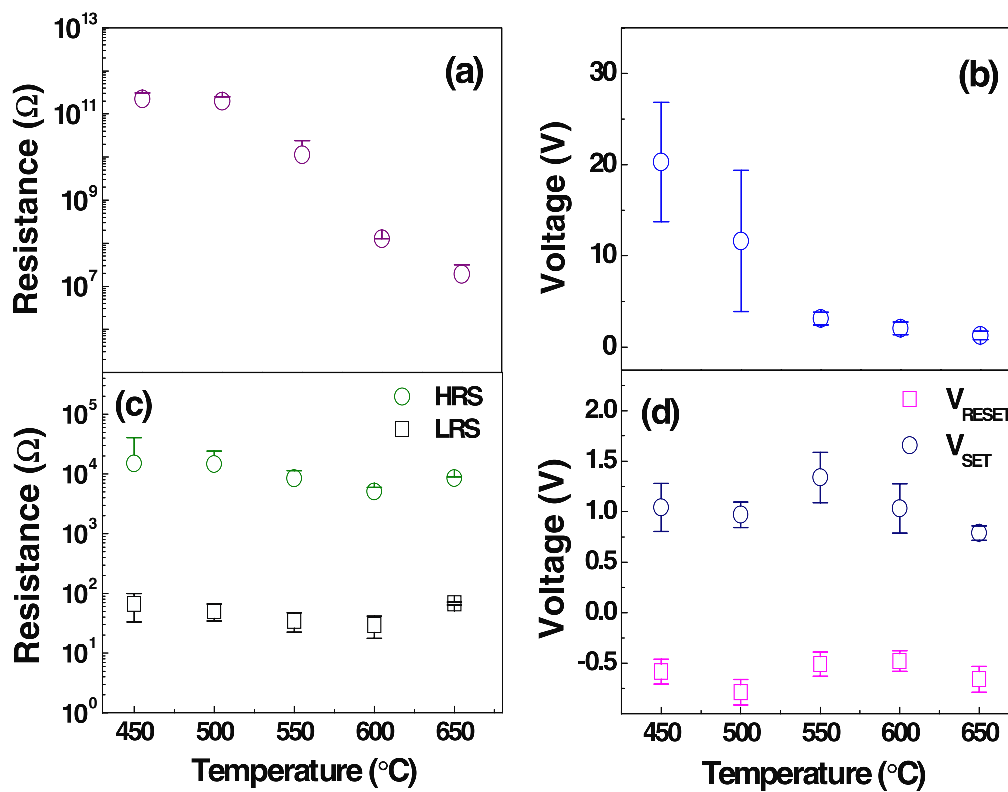

Figure 9. Plots of (*a*) initial resistance versus annealing temperature, (*b*) forming voltage versus annealing temperature, (*c*) R_{HRS} and R_{LRS} versus annealing temperature, and (*d*) programming voltages (V_{SET} and V_{RESET}) versus annealing temperature for BCFO thin films.

Acknowledgments

The authors acknowledge the financial support from the Chinese Academy of Sciences (CAS), the State Key Project of Fundamental Research of China (973 Program), the National Natural Science Foundation of China, the Zhejiang Qianjiang Talent Project, the Zhejiang and Ningbo Natural Science Foundations.

References

[1] Lauters M, McCarthy B, Sarid D and Jabbour G E 2006 *Appl. Phys. Lett.* **89** 013507

[2] Lai Y S, Tu C H, Kwong D L and Chen J S 2005 *Appl. Phys. Lett.* **87** 122101

[3] Jo S H, Kim K H and Lu W 2009 *Nano Lett.* **9** 870

[4] Zhuge F, Dai W, He C L, Wang A Y, Liu Y W, Li M, Wu Y H, Cui P and Li R W 2010 *Appl. Phys. Lett.* **96** 163505

[5] He C L *et al* 2009 *Appl. Phys. Lett.* **95** 232101

[6] Zhuang X, Chen Y, Liu G, Li P, Zhu C, Kang E, Neoh K, Zhang B, Zhu J and Li Y 2010 *Adv. Mater.* **22** 1731

[7] Yoo I K, Kang B S, Park Y D, Lee M J and Park Y 2008 *Appl. Phys. Lett.* **92** 202112

[8] Yang W Y and Rhee S W 2007 *Appl. Phys. Lett.* **91** 232907

[9] Zhou P, Shen H, Li J, Chen L Y, Gao C, Lin Y and Tang T A 2010 *Thin Solid Films* **518** 5652

[10] Shang D S, Shi L, Sun J R, Shen B G, Zhuge F, Li R W and Zhao Y G 2010 *Appl. Phys. Lett.* **96** 072103

[11] Kim D S, Kim Y H, Lee C E and Kim Y T 2006 *Thin Solid Films* **515** 2573
[12] Wang Y *et al* 2010 *Nanotechnology* **21** 045202
[13] Lee J, Choi H, Seong D, Yoon J, Park J, Jung S, Lee W, Chang M, Cho C and Hwang H 2009 *Microelectron. Eng.* **86** 1933
[14] Szot K and Speier W, Bihlmayer G and Waser R 2006 *Nature Mater.* **5** 312
[15] Yin K, Li M, Liu Y, He C, Zhuge F, Chen B, Lu W, Pan X and Li R W 2010 *Appl. Phys. Lett.* **97** 042101
[16] Chen S and Wu J 2010 *Thin Solid Films* **519** 499
[17] Rivera J V and Schmid H 1997 *Ferroelectrics* **204** 23
[18] Wang J *et al* 2003 *Science* **299** 1719
[19] Ranjith R, Prellier W, Cheah J W, Wang J and Wu T 2008 *Appl. Phys. Lett.* **92** 232905
[20] Wang X, Liu H and Yan B 2009 *J. Eur. Ceram. Soc.* **29** 1183
[21] Lee D, Kim M G, Ryu S, Jang H M and Lee S G 2005 *Appl. Phys. Lett.* **86** 222903
[22] Huang F, Lu X, Lin W, Wu X, Kan Y and Zhu J 2006 *Appl. Phys. Lett.* **89** 242914
[23] Shannigrahi S R, Huang A, Chandrasekhar N, Tripathy D and Adeyeye A O 2007 *Appl. Phys. Lett.* **90** 022901
[24] Qi X, Dho J, Tomov R, Blamire M G and MacManus-Driscoll J L 2005 *Appl. Phys. Lett.* **86** 062903
[25] Kim J K, Kim S S, Kim W, Bhalla A S and Guo R 2006 *Appl. Phys. Lett.* **88** 132901
[26] Naganuma H, Miura J and Okamura S 2009 *J. Electroceram.* **22** 203
[27] Singh S K, Maruyama K and Ishiwara H 2007 *Appl. Phys. Lett.* **91** 112913
[28] Kawae T, Terauchi Y, Tsuda H, Kumeda M and Morimoto A 2009 *Appl. Phys. Lett.* **94** 112904
[29] Hu G D, Fan S H, Yang C H and Wu W B 2008 *Appl. Phys. Lett.* **92** 192905
[30] Quan Z, Liu W, Hu H, Xu S, Sebo B, Fang G, Li M and Zhao X 2008 *J. Appl. Phys.* **104** 084106
[31] Gao F, Qiu X Y, Yuan Y, Xu B, Wen Y Y, Yuan F, Lv L Y and Liu J M 2007 *Thin Solid Films* **515** 5366
[32] Yang H, Wang Y Q, Wang H and Jia Q X 2010 *Appl. Phys. Lett.* **96** 012909
[33] Fang L, Liu J, Ju S, Zheng F, Dong W and Shen M 2010 *Appl. Phys. Lett.* **97** 242501
[34] Kumar K R and Satyam M 1981 *Appl. Phys. Lett.* **39** 898
[35] Steinhauser J, Faÿ S, Oliveira N, Vallat-Sauvain E and Ballif C 2007 *Appl. Phys. Lett.* **90** 142107
[36] Yang K G, Zhang Y L, Yang S H and Wang B 2010 *J. Appl. Phys.* **107** 124109
[37] Chen X, Wu G and Bao D 2008 *Appl. Phys. Lett.* **93** 093501
[38] Waser R, Dittmann R, Staikov G and Szot K 2009 *Adv. Mater.* **21** 2632
[39] Li M, Zhuge F, Zhu X, Yin K, Wang J, Liu Y, He C, Chen B and Li R W 2010 *Nanotechnology* **21** 425202
[40] Yang Y C, Pan F, Liu Q, Liu M and Zeng F 2009 *Nano Lett.* **9** 1636
[41] Bid A, Bora A and Raychaudhuri A K 2006 *Phys. Rev.* B **74** 035426
[42] Lee J S and Joo S K 2002 *Appl. Phys. Lett.* **81** 2602
[43] Lee M-J, Han S, Jeon S H, Park B H, Kang B S, Ahn S-E, Kim K H, Lee C B, Kim C J, Yoo I-K, Seo D H, Li X-S, Park J-B, Lee J-H and Park Y *Nano Lett.* **9** 1476